

CDC-42 encodes dynamically stable asymmetries in the *C. elegans* zygote via an incoherent feed-forward loop

Ondrej Maxian, Cassandra Azeredo-Tseng, . . . , and Edwin Munro

April 17, 2024

1 Introduction

Cell polarity is essential for many aspects of organismal development and physiology, including stem cell dynamics, directional cell migration, and asymmetric cell division (Dewey et al., 2015; Goldstein and Macara, 2007; Ierushalmi and Keren, 2021; Maître et al., 2016). For most cells, the first step in polarization involves a symmetry-breaking response to a transient localized cue that creates asymmetric distributions of specific molecules or molecular activities. The mechanisms that underlie cellular symmetry-breaking have been extensively explored (Li and Bowerman, 2010), but mechanisms that maintain polarity as a dynamically stable state with a fixed boundary position have only recently come under scrutiny (Sailer et al., 2015; Gross et al., 2019).

On a large scale, a cell’s polarity state is encoded by asymmetric distributions of protein molecules, which are shaped by smaller-scale processes like binding, diffusion, and active transport. In *C. elegans*, polarity is encoded by the distribution of two distinct groups of (highly conserved) polarity proteins: anterior PARs (aPARs), which include the scaffold PAR-3, adaptor PAR-6, atypical kinase PKC-3, and GTPase CDC-42, and posterior PARs (pPARs), which include the RING-domain containing protein PAR-2 (Bland et al., 2023), kinase PAR-1, tumor suppressor LGL-1, and CDC-42 GAP CHIN-1 (Lang and Munro, 2017).

Wild-type embryos polarize in two distinct phases termed “establishment” and “maintenance” (Cuenca et al., 2003). The mechanisms that underlie symmetry-breaking during polarity establishment have been well-studied (Cowan and Hyman, 2007; Munro and Bowerman, 2009). Near the end of meiosis, PAR-3, PAR-6 and PKC-3 are uniformly distributed at the cortex, where they prevent cortical association of PAR-1, PAR-2 and LGL-1 (Schonegg and Hyman, 2006; ?). One mode of symmetry-breaking involves the local inhibition of actomyosin contractility near the sperm MTOC,

which triggers cortical flows that transport F-actin, myosin II, PAR-3/PAR-6/PKC-3, and other cortically associated factors towards the anterior pole, resulting in their mutual restriction to an anterior cap (Munro et al., 2004; Rodriguez et al., 2017). Posterior depletion of PAR-3/PAR-6/PKC-3 then allows PAR-1, PAR-2 and LGL-1 to associate with a complementary posterior domain. Actomyosin contractility and cortical flow during polarity establishment require the small GTPase Rho-1 (Schonegg and Hyman, 2006; Motegi and Sugimoto, 2006), and in fact the sperm cue acts via Aurora A kinase (AIR-1) to locally inhibit Rho through the Rho GEF Ect-2 (Motegi and Sugimoto, 2006; Tse et al., 2012; Longhini and Glotzer, 2022; Kapoor and Kotak, 2019). A second mode of symmetry-breaking has also been described in which sperm astral microtubules promote local association of Par-2 with the posterior cortex (Motegi et al., 2011).

While the mechanisms that break symmetry are by now well understood, it remains unclear what *stops* symmetry breaking. If the system is programmed to amplify an initial polarizing cue, what sets the limit of amplification? The by now standard mechanism is that anterior (CDC-42/PAR-3/PAR-6/PKC-3) and posterior proteins (PAR-1/PAR-2/LGL-1) form a bistable reaction diffusion system by competing for residence at the cortex/plasma membrane such that one or the other but not both win locally. Theoretical studies suggest that in principle such a mechanism could stabilize the AP boundary after establishment phase cortical flows cease, or in embryos that lack cortical actin or myosin (Mori et al., 2008; Dawes and Munro, 2011; Goehring et al., 2011; Lang et al., 2023). These mechanisms by themselves cannot, however, shift the boundary on realistic timescales (Lang et al., 2023), which is why flow is required.

In the presence of flow, it is still unknown what sets a limit to boundary progression. Recent work showed that, assuming an intrinsic self limit to contractility, the boundary can be pinned, with the position set by total amount of each PAR protein (Gross et al., 2019; Goehring et al., 2011). But the self-limiting nature of the flow remains a mystery. In wild type embryos, myosin accumulates at the anterior in a cap that takes up about 50% of the embryo, and myosin flows from the posterior half of the embryo into the anterior cap. Despite the flow of myosin and the consequent A/P asymmetry in contractility, the cap maintains a fixed size (it does not contract), and the flow profile in the anterior is roughly zero (Sailer et al., 2015). Moreover, ectopic accumulation of Myosin II during maintenance in PAR-2 mutants is associated with abnormal posterior-directed cortical flows and rapid redistribution of Par proteins (Munro et al., 2004), suggesting that the distribution of myosin, in addition to the PAR proteins, guides the steady state.

While we will show that the self-limiting nature of contractility applies in both establishment

and maintenance phase, our focus in particular will be on maintenance, which requires CDC-42 to maintain asymmetries set up during establishment (Kay and Hunter, 2001; Gotta et al., 2001; Aceto et al., 2006; Schonegg and Hyman, 2006; Motegi and Sugimoto, 2006). GFP-tagged CDC-42 becomes anteriorly enriched during polarity establishment, and studies with a GFP-tagged biosensor suggest that the active (GTP-bound) form of CDC-42 may be similarly enriched during maintenance phase (Kumfer et al., 2010). Binding of CDC-42 to the conserved semi-Crib domain of PAR-6 is required for cortical association of PAR-6/PKC-3 during maintenance (Aceto et al., 2006), and PKC-3 is in an active state only when bound to CDC-42 (Sailer et al., 2015; Lang and Munro, 2017; Rodriguez et al., 2017). CDC-42 also acts through MRCK-1, a *C. elegans* orthologue of the mammalian Myotonia Dystrophy-related CDC-42-binding kinase MRCK, to promote asymmetric cortical recruitment of myosin II (Kumfer et al., 2010). There is also evidence that CDC-42 promotes asymmetric enrichment of F-actin during maintenance phase (REF?), but the underlying mechanism remains poorly understood. More generally, it remains unclear how these distinct outputs of CDC-42 are integrated to dynamically stabilize the AP boundary at a fixed axial position and limit contractility.

In this study, we combine experiments and theoretical modeling to show that boundary progression can be stalled when distinct outputs of CDC-42 have different effects on contractility. By extending both establishment and maintenance phases, we show that the boundary position is in fact stable, regardless of the cell cycle phase. We then demonstrate, through experiments with a temperature sensitive ECT-2 gene (Zonies et al., 2010), that the steady state observed at the end of maintenance phase can be reproduced even when establishment fails through a maintenance-phase rescue process, revealing that maintenance phase biochemistry encodes a dynamically stable attractive state. To understand how the PAR protein circuit (which involves CDC-42) interacts with myosin contractility to limit the extent of contractility, we introduce a continuum model. Without a self-limiting character to the flow, the boundary either contracts all the way to the end of the embryo, or slowly moves to the embryo interior over a timescale an order of magnitude longer than maintenance phase. To find the missing model component, we return to experiments, which demonstrate that branched actin in the anterior acts to reduce tension and prevent excessive contraction, similar to behavior observed previously in other systems (Muresan et al., 2022; Yang et al., 2012). Our model reveals that adding a threshold of CDC-42, above which branched actin is produced, is sufficient to reproduce the initial and latter stages of rescue, with the caveat that additional assumptions about branched actin are required to reproduce all experimental observations.

2 The distinction between establishment and maintenance

- (A) Cell cycle progression controls a regime change from rho-dependent contractility to CDC-dependent contractility.
- (B) Relaxation of pseudo-cleavage is a marker for this transition (so is onset of centration).
- (C) CDC-42 also involved in biochemistry (complexing with PAR-6/PKC-3 to inhibit pPARs), so biochemistry and contractility are intimately coupled in maintenance phase (different from establishment phase where rho has its own pulsatile/oscillatory dynamics).

3 The steady state of maintenance phase

It has been previously observed that embryos in late-maintenance phase exhibit a steady pattern of anterior-directed cortical flow (see (Sailer et al., 2015, Fig. 2)). Yet, despite the anterior-directed contractility, the A/P boundary in late maintenance appears to be stable. It remains unclear if this pattern of flow is a consequence of establishment-phase patterning of myosin (Munro et al., 2004), or if the pattern of flow is merely transient and would eventually stop if the cell cycle extended long enough. In this section, we establish that the pattern of flow and myosin profile in maintenance phase are in fact robust (to changes in establishment phase contractility) and long-lasting (if maintenance phase is extended); in other words, we seek to show that maintenance-phase biochemistry encodes an attractive steady state.

3.1 Extending maintenance phase establishes boundary position as stable

The pinning of the myosin boundary and subsequent decrease in the speed of flow hint that the cell has a built-in mechanism to prevent the boundary from contracting off the end of the embryo. But is it really possible to maintain a steady myosin intensity profile in the presence of a persistently anterior-directed flow?

To probe whether the myosin intensity and patterns of flow we see in late maintenance phase are truly steady states, we extend maintenance phase by treating wild-type embryos with CDK-1 (RNAi). Marking the start of maintenance phase by the end of pseudo-cleavage, and the end of maintenance phase by the onset of cytokinesis, we obtain a window of roughly 8–10 minutes per cell, in which we characterize the myosin intensity and flow speeds (see SI). Later stages of the

extended maintenance show a relatively stable position of the myosin boundary (it in fact expands towards the posterior slightly) and a persistent anterior-directed flow which tends to achieve a maximum (magnitude) just posterior of the peak myosin location. Because the myosin intensity and flow speeds in *CDK-1* (RNAi) never resemble those of wild-type, it is clear that interfering with CDK-1 affects more than just the cell cycle, and it is impossible to say concretely that the specific flow and myosin profiles in late maintenance are “steady.” Nevertheless, we can say definitively that a persistent anterior-directed flow does *not* lead to further contraction of the boundary when maintenance is extended.

3.2 Maintenance phase rescue

In addition to stabilizing asymmetries that are set up during establishment phase, the biochemical and mechanical interactions in maintenance phase can also rescue a steady polarized state. While this has been observed in previous studies in *ect-2* mutants (Zonies et al., 2010; Tse et al., 2012), which cannot activate Rho and consequently lack myosin functionality during establishment phase, it has yet to be shown that the steady polarized state that results is the same as in wild-type embryos. To establish this, we systematically image rescue of symmetry breaking in temperature-sensitive *ect-2* mutants, marking the beginning of maintenance phase via the transition of myosin from large to small clusters, and the end of maintenance phase as the onset of embryo rotation prior to cytokinesis. This gives a roughly four minute window of maintenance phase for each embryo, in which we track the average myosin intensity profile and flow speed.

3.2.1 Rescue requires MRCK

Need to show that it cannot happen without myosin flows.

3.3 Model reveals existing mechanisms cannot explain rescue

Our goal in this section is to explore existing literature mechanisms for how maintenance phase biochemistry could set an attractive steady state. At first glance, it appears that the phenomenon of maintenance phase rescue is a consequence of an instability of the underlying system; a small perturbation in the myosin concentration could induce an anterior-directed flow, which drives the system to the polarized state. Here we systematically exclude this by considering a model of myosin alone and showing that spontaneous symmetry breaking is not possible with realistic parameters. We then consider PAR proteins, showing that, while the PAR circuit we consider can maintain

a stable polarized state with a fixed boundary position, the time required to set up this state is prohibitively long, and myosin-directed flows are required. Finally, we consider a combination of myosin-driven flows *and* PAR proteins. This model allows us to reproduce the initial stages of maintenance phase rescue, but it cannot explain the sudden slow-down in flow speeds and pinning of the myosin boundary.

3.3.1 Myosin without additional feedback cannot spontaneously polarize

We first explore the dynamics of myosin alone, which we describe in terms of a one-dimensional spatially and temporally varying field $M(x, t)$ which evolves according to the advection-diffusion-reaction equations (Bois et al., 2011)

$$\partial_t M + \partial_x(vM) = D_M \partial_x^2 M + k_M^{\text{on}} M_{\text{cyto}} - k_M^{\text{off}} M \quad (1a)$$

$$\gamma v = \eta \partial_x^2 v + \partial_x \sigma_a(M) \quad (1b)$$

The velocity field (1b) comes from the assumption that myosin generates an active stress $\sigma_a(M)$, which combines with the viscous stress to give the total cortical stress $\sigma = \eta \partial_x v + \sigma_a(M)$. The force balance equation in the fluid says that the force due to stress must be balanced by the drag force, $\gamma v = \partial_x \sigma$, where γ is the drag coefficient. Combining the force balance with the stress expression gives the velocity equation (1b), which can also be rewritten in terms of the “hydrodynamic lengthscale” $\ell = \sqrt{\eta/\gamma} \approx 14 \mu\text{m}$, which is essentially the lengthscale on which a local increase in the myosin field will pull in neighboring molecules (Mayer et al., 2010). As in (Bois et al., 2011), we ignore the elastic part of the stress, since the actomyosin cortex is purely viscous on timescales longer than the cortical turnover time (Mayer et al., 2010).

In the case when diffusion of myosin is negligible and all myosin is bound to the membrane, the stability analysis in the SI shows that the dynamics are unstable when the flow carries myosin molecules a distance larger than the hydrodynamic lengthscale, i.e., $v/k_M^{\text{off}} > \ell$. Substituting $\ell \approx 14 \mu\text{m}$, we plot the velocity threshold for instability as a function of myosin lifetime in Fig. S4. For realistic lifetimes on the order 5–20 s, the minimum flow speed to generate instability is about $40 \mu\text{m}/\text{min}$, which is much faster than ever observed *in vivo*. Thus the dynamics of maintenance phase rescue are not due to myosin instabilities.¹

¹We note a distinction here between maintenance and establishment phase. In the latter, instabilities in the dynamics of rho combine with delayed negative feedback to yield pulsatile dynamics (Nishikawa et al., 2017; Michaux et al., 2018; Michaud et al., 2022). The connection between these pulsatile dynamics and the large-scale flows that

3.3.2 Basic maintenance-phase biochemistry circuit

Because the dynamics of myosin alone are insufficient to generate instability, PAR proteins must be essential for rescue to occur (Zonies et al., 2010). We consequently introduce a model of maintenance phase biochemistry based on the diagram in Fig. ??, which in turn comes from (Lang and Munro, 2017, Fig. 2). On the anterior side, we have three distinct protein species: PAR-3 (A), CDC-42 (C), and PAR-6/PKC-3 (K), each of which has a separate function. The posterior PARs (PAR-2, PAR-1, and CHIN-1) can be lumped into one species (denoted by P), which antagonizes both PAR-3 and CDC-42. The dimensional equations which describe the circuit are

$$\partial_t A_1 = D_A \partial_x^2 A_1 + (k_A^{\text{on}} + k_A^+ f_A^+(A)) A_{\text{cyto}} - k_A^{\text{off}} A_1 \quad (2a)$$

$$+ 2k_A^{\text{dp}}(P) \hat{A}_2 - 2k_A^p \hat{A}_1^2 + \sum_{n=3}^N (A_n - k_A^{\text{dp}}(P) A_1 A_{n-1})$$

$$\partial_t A_n = k_A^p A_1 (A_{n-1} - A_n) - k_A^{\text{dp}}(P) (A_n - A_{n+1}) \quad N > n \geq 2 \quad (2b)$$

$$\partial_t A_N = k_A^p A_1 A_{N-1} - k_A^{\text{dp}}(P) A_N \quad (2c)$$

$$\partial_t C = D_C \partial_x^2 C + k_C^{\text{on}} C_{\text{cyto}} - k_C^{\text{off}} (1 + r_{\text{PC}} P) C \quad (2d)$$

$$\partial_t K = D_K \partial_x^2 K + r_{\text{ACK}} C \delta_{A>A_0} K_{\text{cyto}} - k_K^{\text{off}} K \quad (2e)$$

$$\partial_t P = D_P \partial_x^2 P + k_P^{\text{on}} P_{\text{cyto}} - k_P^{\text{off}} (1 + r_{\text{KP}} K) P \quad (2f)$$

The PAR-3 equations (2a)–(2c) describe the dynamics of PAR-3 oligomerization (an oligomer of size n denoted by A_n), for which we use the model developed in (Lang et al., 2023). As discussed in detail there, the combination of oligomerization and positive feedback (through the term $k_A^+ f_A^+(A)$) imparts intrinsic bistability to the system. This bistability is strengthened when pPARs are included; through the term $k_A^{\text{dp}}(P)$, these posterior PARs promote depolymerization of PAR-3.

PAR-3 also gates the association of CDC-42 with PAR-6/PKC-3 (K), which is a complex that inhibits all posterior PARs (Lang and Munro, 2017). To model this, we work off the observations in (Sailer et al., 2015), which reveal that PAR-6/PKC-3 are recruited to the membrane by CDC-42, provided that there is a sufficient concentration (roughly 10% of the enriched anterior level) of PAR-3 on the membrane. Thus the total loading term in (2e) is proportional to the CDC-42 concentration times the cytoplasmic concentration of K , provided the PAR-3 concentration satisfies $A > A_0$. The other two equations (for CDC-42 and pPARs) are straightforward: we assume a basal

establish polarity is still unknown.

rate of binding and unbinding, with an unbinding rate which is linearly enhanced by the inhibitor (pPARs for CDC-42 and PKC-3 for pPARs). In the supplemental appendix, we nondimensionalize (2), then use sets of existing experimental observations about the relative amount of each species on the anterior/posterior side of the embryo, as well as estimates of the amounts in the cortex vs. cytoplasm, to constrain the unknown parameters.

3.3.3 PAR proteins without contractility amplify asymmetries, but too slowly

In previous work on PAR-3 (Lang et al., 2023), we demonstrated that the diffusion of the smaller oligomer sizes (monomers in our model) sets a unique boundary position. In Fig. ??, we demonstrate that this with the full biochemistry by simulating the contraction of a PAR-3 domain that initially takes up 90% of the embryo. The boundary shifts because a high concentration of pPARs shifts the local equilibrium of PAR-3 oligomerization towards the monomer state, which makes bistability impossible (Lang et al., 2023). Consequently, we observe contraction of the PAR-3 domain, with a peak that grows over time, and expansion of the PAR-2 domain, both of which eventually reach a steady state. The concentration of PAR-2 at the edge of the domain decreases over time, which suggests that cytoplasmic depletion might be responsible for pinning the boundary. To demonstrate that a fixed pool of protein is key to arresting posterior domain expansion, in the right panel of Fig. ?? we simulate with a cytoplasmic pool that is “frozen” at its value at $t = 10$ mins. The result is an anterior domain which shrinks at a constant rate with constant peak concentration, and a posterior domain which expands at a constant rate with the same concentration at the edge. Given enough time, the posterior domain invades the entire embryo length.

In (Lang et al., 2023), we showed that the diffusion-controlled shift of the PAR-3 boundary occurs on timescales of hours, meaning that the boundary never reaches a steady position in practice. This is confirmed in Fig. ??, which shows that cytoplasmic depletion can only act rapidly to stop boundary progression if the initial boundary size is close to the steady state. The simulation in Fig. ??(a), which starts at 90% PAR-3 enrichment takes some two hours to reach the steady state; while a simulation starting at 50% PAR-3 enrichment takes only 5–10 minutes. In order to reproduce rescue, we need to introduce cortical flows that initially shift the boundary at a faster initial rate. If these cortical flows are then arrested, cytoplasmic depletion can then prevent the boundary from shifting, leading to a steady state.

3.3.4 Coupling contractility to biochemistry reproduces initial stages of rescue

Because neither myosins nor PAR proteins can rescue maintenance phase asymmetries by themselves, there must be an interaction with PAR proteins that amplifies gradients in contractility to rescue the correct polarized state. To account for this, we add the myosin dynamics (1) to the biochemistry system (2). In doing this, we also incorporate advective terms that ensure that each protein moves with the local cortical velocity (Illukkumbura et al., 2023), and make CDC-42 a promoter of myosin. The equations corresponding to this situation are a straightforward extension of (1) and (2), and we therefore confine them to the supplemental material, where we give a non-dimensional version and fit the unknown parameters.

In Figure ?? shows the results when we the parameters to match the experimentally-measured initial speeds of rescue. The left panel shows the dynamics of the simulation from $t = 0$ (lightest colors) to $t = 7.5$ mins (darkest colors), while the right panel shows the myosin boundary position (0 is the anterior pole, 1 is the posterior pole) and the flow speeds over time. Our statistics show the beginning of the rescue process, where an initially peaked profile of PAR-2 invades the anterior domain, concentrating anterior PARs in the middle and thereby increasing the concentration of pPARs in the posterior. As a result of this, CDC-42 gets inhibited in the posterior, which gives a gradient of myosin from posterior to anterior. The gradient of myosin generates a flow which further compacts the anterior domain. The timescale of this compaction is much faster than without flows (Fig. ??), and indeed occurs on a timescale of minutes and not hours.

While our model reproduces the initial stages of the rescue process, there is no mechanism in it to halt the advancing myosin front. With the correct model parameters, the tendency of flow to concentrate the aPARs overwhelms the effect of cytoplasmic depletion (which tends to slow the boundary motion). As a result, the boundary contracts with nothing to slow it down. Indeed, in the limit as time goes to infinity, we expect one peak of aPARs and myosin at the anterior pole, which is in sharp contrast to our experimental result which showed a sharp drop in the anterior-directed flow speed in the late stages of maintenance phase (see inset of Fig. ??).

4 Branched actin as a brake on contractility

Our modeling so far identified two regimes of behavior, depending on the sensitivity of myosin to the CDC-42 concentration. Roughly speaking, if CDC-42 promotes myosin at a rate much smaller than the basal rate (0 in Fig. ??), the cytoplasmic dynamics are sufficient to stop the pPARs from

invading too far into the anterior domain. But this model has to be discarded because the dynamics occur over unrealistically long timescales. To match the speed of rescue, CDC-42 has to promote myosin at a rate much larger than the basal rate, which leads to fast flows and (in this model) a rapid concentration of the anterior domain into a peaked profile at the anterior pole (Fig. ??). Thus, we are missing an important interaction that slows down the advancing myosin peak, rapidly dropping the flow speed and allowing cytoplasmic depletion to pin the boundary. This interaction is the focus of this section.

4.1 Reduced contractility in anterior is correlated with branched actin

In Fig. ?? we show the myosin intensity and flow speed over 30 second intervals of maintenance phase rescue, and compare the result to the steady myosin intensities and flow speeds observed in wild-type embryos (Sailer et al., 2015). The myosin peak initially grows in size advances rapidly towards the anterior, but after about three minutes it stops growing and becomes pinned at about 40% embryo length. The pinning of the myosin peak corresponds to a decrease in the maximum flow speed from about $4.5 \mu\text{m}/\text{min}$ (from 2:00 to 3:30) to $2 \mu\text{m}/\text{min}$ in the last 30 seconds of maintenance phase (3:30 to 4:00, see the inset of Fig. ??). In the last 30 seconds of maintenance phase, the flow profile in *ts ect-2* embryos is roughly the same as that observed during late maintenance phase in wild-type embryos. The myosin intensity appears quantitatively different, but has the same fundamental shape: there is a gradient of myosin in both the anterior and posterior, with a maximum occurring at around 40% of the embryo length. These results establish that the biochemical circuit governing maintenance phase can amplify small residual asymmetries from establishment phase, and that the resulting polarized state is independent of what comes before maintenance.

4.2 Experiments in arx-2 (RNAi) embryos establish a hyper-contractile state

Figure we want to make for this section:

- (a) Pictures of wild-type vs. arx-2 (RNAi) embryos in late maintenance
- (b) Measurements of myosin peak in maintenance (left panel of Fig. ??; put flows in SI if at all)
- (c) Pictures of ect-2 (ts) with and without arx-2 (RNAi) in early and late maintenance
- (d) Kymograph of rescue with and without arx-2 (RNAi)
- (e) Pictures of control vs. arx-2 (RNAi) for embryos *with nocodazole* treatment
- (f) Myosin intensity & flow in control vs. arx-2 (RNAi) *with nocodazole* (Fig. ?? here)

We hypothesize that branched actin might stop the anterior cap from becoming hyper-contractile. To test this hypothesis, we deplete wild type embryos of arx-2, a protein which activates the arp

2/3 complex and the assembly of branched actin. Figure ?? shows the average myosin intensity and flow profiles over the last three minutes of maintenance phase in wild-type (red) and arx-2 (RNAi) treated embryos (blue). While the wild-type intensity seems to be roughly stalled at a boundary position 40% of the embryo length, the arx-2 (RNAi) embryos demonstrate hyper-contractility, with a myosin peak that shifts to the anterior (and increases) over time.

The flow measurements in *arx-2* (RNAi) embryos are chaotic and noisy because the hypercontractile anterior cap is not always positioned directly on the anterior pole, so flows can be generated off the A/P axis. In Fig. ??, we show the average flow speeds in embryos where the A/P flow dominates other directions (6 of the 12 embryos). These flows have a maximum speed around 2.5–4 $\mu\text{m}/\text{min}$. Unlike the wild-type profile, whose point of maximum flow and stall point are roughly constant in time, the *arx-2* (RNAi) flow profiles show no stall point, are larger in magnitude, and have a local maximum which is positioned far to the anterior of the wild-type.

We hypothesized that the chaotic and noisy flow speeds in *arx-2* (RNAi) embryos were a result of the smaller anterior cap being pulled and pushed around by forces from the mitotic spindle. Because of this, we applied nocodazole, a drug which depolymerizes microtubules, and observed the resulting dynamics. Interestingly, nocodazole treatment of wild type embryos appears to remove the posterior-directed flow earlier in early maintenance phase (Fig. ??) (Sailer et al., 2015). In late maintenance, however, the dynamics are relatively unchanged with nocodazole treatment, with a peak in the myosin concentration around 40% embryo length and a maximum flow speed of 2 $\mu\text{m}/\text{min}$ at 60% embryo length (blue lines in Fig. ??).

In *arx-2* (RNAi) embryos, nocodazole treatment significantly improved the patterns of flow, confining them to the A/P axis and allowing us to extract meaningful information. Similar to the case without nocodazole, embryos treated with arx-2 (RNAi) and nocodazole showed a hypercontractile anterior myosin cap (Fig. ??), with the cap continuing to contract over time to the very edge of the anterior domain. The contraction of the cap corresponded with marked increases in flow speed during maintenance, so that flows went from 1.5 $\mu\text{m}/\text{min}$ during the third minute before anaphase onset to 3–4 $\mu\text{m}/\text{min}$, with the point of maximum flow occurring at 40% embryo length instead of 60% (Fig. ??). Thus, regardless of the presence of microtubules, depletion of arx-2 by RNAi leads to a hypercontractile state with a larger velocity and a cap which tends to fall off the edge of the embryo, similar to what we observed in simulations in Fig. ???. We now propose a model for how branched actin could inhibit contractility and lead to the formation of a stable boundary.

4.3 Model of branched actin correctly reproduces rescue dynamics

Figure we want to make for this section:

- (a) Schematic showing ways we consider branched actin working
- (b) Simulation with tension reduction showing boundary stops (and remaining issues; Fig. ?? here)
- (c) “Best” simulation reproducing all trends (Fig. ?? here).

To model branched actin, we work off the following two important observations from our maintenance-phase rescue experiments: first, the pinning of the myosin domain and drop in velocity happen quite abruptly, and second, the rapid drop in velocity is *not* accompanied by strong changes in the myosin concentration profile (Fig. ??). These observations together suggest that there is an ultra-sensitive dependence of contractility (not myosin concentration) on branched actin. As rescue progresses, branched actin becomes active on the anterior, providing a “brake” which slows down contractility and progression of the boundary.

To translate our hypothesis into our model, we make the following assumptions,

1. To activate branched actin, we assume a threshold of CDC-42 above which branched actin is created. The threshold is reached roughly when the A/P boundary reaches the middle of the cell.
2. Branched actin assembly is autocatalytic, since new branches become sites for additional branches.
3. Branched actin unbinds from the cortex with characteristic rate k_R^{off} (about 8 s lifetime).
4. While branched actin does not diffuse in the cortex, polymerization of actin leads to a spreading out of the branched network, and so we include nonzero diffusivity.
5. Branched actin inhibits contractility.

The first four assumptions lead to the advection-diffusion-reaction equation

$$\partial_t R + \partial_x(vR) = D_R \partial_x^2 R + (r_{\text{CR}} \max(C - C_R, 0) + r_{\text{RR}} R) R_{\text{cyto}} - k_R^{\text{off}} R \quad (3a)$$

for the evolution of branched actin (R) in time and space. For the fifth assumption, we postulate a simple relationship for how branched actin impacts contractile stress

$$\sigma_a = \frac{\sigma_0 M}{1 + r_{R\sigma} R}. \quad (3b)$$

We use division of the stress instead of subtraction because, as the branched actin concentration goes to infinity, we expect the tension to approach zero, as was shown to be the case *in vitro* using laser ablation (Muresan et al., 2022). In the SI, we give the dimensionless form of (3a) and (3b) and estimate the unknown parameters.

The dynamics of rescue in this case are shown in Fig. ???. In the early stages of rescue, we see a concentration of myosin and CDC-42 into an interior peak which grows over time. Once the concentration of CDC-42 at the peak exceeds the threshold $C_R = 0.25$, branched actin is produced. This causes an immediate drop in contractility within the peak (see the active stress profile at intermediate times), which leads to a leveling out of the anterior profiles of CDC-42 and myosin (weaker flows in the anterior allow CDC-42 to diffuse over). Following this, branched actin builds up on the anterior. The boundary stops moving when the tension on the anterior balances the tension on the posterior, leaving an intermediate zone of contractility at around 60% embryo length.

A necessary feature of our simulations is the threshold dependence of branched actin production on CDC-42 activity. In the SI, we demonstrate that simulations without a threshold give velocity profiles which build up from zero at $t = 0$ to a plateau value later in time. That is, without a threshold dependence, it is impossible to reproduce the experimental result of a velocity which suddenly *decreases* when the boundary penetrates the interior.

Nevertheless, while simulations with a threshold qualitatively reproduce what we observe in maintenance phase rescue (the anterior boundary progresses and then stops), there are two details that do not match the experiments. First, as soon as branched actin inhibits contractility, the myosin concentration profile tends to flatten out in the anterior (it is no longer peaked). This is not what we see in the rescue experiments (data in Fig. ??), where myosin stays peaked after the boundary stops moving. Second, the flow profile from simulations is symmetric about the myosin peak with a flow of about $1 \mu\text{m}/\text{min}$ coming from *both* the anterior and posterior into the zone of contractility. This is also not what we observe in experiments, where the flow profile is essentially flat in the anterior (up to 40% embryo length), and anterior-directed in the posterior (see Fig. ??). In the following sections, we add to our model to try to address these two issues.

4.3.1 Detail 1: reproducing the myosin profile

Let us consider first the issue of the myosin concentration profile. What is missing from our inhibition model that causes myosin to be flat in the anterior? We previously saw that inhibition of tension by branched actin inhibits flows in the anterior, which allows diffusion to level out the

anterior CDC-42 profile, which in turn levels out the anterior myosin profile. At steady state, there is a compressive flow in the middle of the embryo, but the speed of the flow (at most $2 \mu\text{m}/\text{min}$ as measured in experiments) is insufficient to concentrate myosin or CDC-42. **Some statement about myosin and CDC-42 distributions.**

We propose two possible explanations to address this issue. First, a simple explanation is that myosin could have a longer lifetime than 8 s, as we can track the large clusters for some 30 s before they disappear. A second possibility is that branched actin could also inhibit myosin directly in the anterior, for example by thickening the cortex and forcing myosin unbinding (which was shown to occur in mouse oocytes (Chaigne et al., 2015)). As shown in the SI, both of these models show a better fit to the data as far as the myosin profile, but neither have a velocity which matches that obtained from experiments, as there is still a backflow in the anterior which results from the reduction of tension and myosin inhibition.

4.3.2 Detail 2: reproducing the (lack of) flow on the anterior

Because there is an enrichment of myosin at the midline relative to the anterior pole, and because branched actin inhibits tension, the results in Fig. ?? show an anterior gradient in tension and a flow from the anterior to the midline. However, in wild-type and *ect-2* (ts) embryos in late maintenance, we never detect a substantial (larger than $1 \mu\text{m}/\text{min}$) flow in the anterior (see Fig. ??), despite the gradient in myosin (and presumably in tension). Put another way, gradients in tension do not translate to flows the same way in the anterior as they do in the posterior, presumably because of branched actin.

Our model equation for velocity (1b) has two addition parameters that model how flow responds to changes in contractility. The parameter that controls the magnitude of the flow obtained for a fixed tension gradient is the drag or friction coefficient γ , and the parameter that controls the response to a given rate of strain ($\partial_x v$) is η . We propose that branched actin could modulate each of these parameters according to the linear relationships

$$\gamma(R) = \gamma_0 (1 + r_{R\gamma} R) \quad \eta(R) = \eta_0 (1 + r_{R\eta} R).$$

These two models, while superficially similar, are at a deeper level quite different. In the case of increased friction, we are proposing that the velocity can rapidly change from negative (in the posterior) to positive (in the anterior), but that the magnitude of the positive velocity in the anterior

is necessarily smaller because the same force on that side generates a smaller velocity than on the posterior. Increased viscosity, by contrast, says that the branched actin network resists changes in strain rate (sharp changes in velocity). By increasing viscosity, we are proposing that the changes in tension on the anterior side cannot induce compressive flows because of viscous resistance.

In the SI, we analyze both of these models, and conclude that either a moderate increase (a factor of 2) in the viscous resistance, or a large increase in the frictional resistance (a factor of 10) in the anterior is sufficient to reproduce the dynamics observed experimentally. A large increase in viscosity results in an anterior flow that cannot rapidly respond to changes in tension, and as such cannot stop the boundary from progressing by slowing the flow. A small increase in friction is simply not large enough to reproduce the experimental flow profile (it still retains the compressive flow in the anterior).

4.3.3 Best case parameters

Our best attempt to reproduce the experimental data is shown in Fig. ???. In this simulation, we add direct inhibition of myosin by branched actin, so that branched actin in the anterior increases the off rate by about 50%. Likewise, we add a viscosity enhancement, so that the viscous resistance in the anterior (with branched actin) is roughly 3 times the posterior (see SI for exact parameters). The dynamics in Fig. ?? (myosin and flow profiles) agree well with those observed experimentally,

5 Discussion

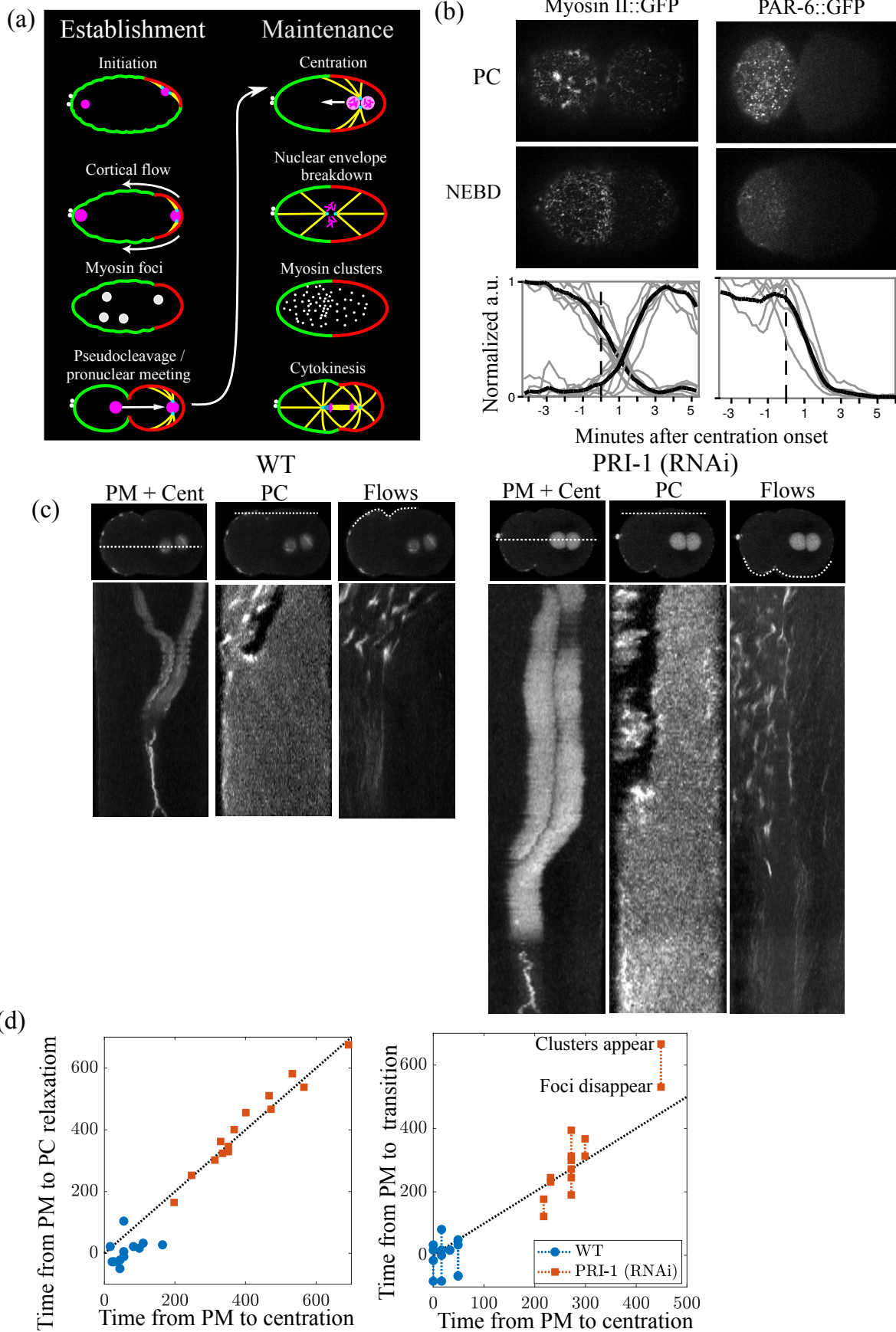


Figure 1: Cell cycle progression controls a regime change from rho-dependent to CDC-42-dependent contractility. (a) Overview of dynamics during establishment and maintenance phase, including key events in the cell cycle. (b) Distributions of non-muscle-myosin II (NMY-2::GFP; left panels) GFP::PAR-6 (right panels) in wild-type embryos at/near the end of pseudocleavage (top panels) or nuclear envelope breakdown (bottom panels). Graphs show the normalized intensity of myosin foci and clusters (left), or PAR-6 clusters (right) over time relative to centration onset. (c) Kymographs showing the correlation between pronuclear meeting and centration (left), pseudocleavage relaxation (middle), and flow into the pseudocleavage (right) in wild type (left) and PRI-1 (RNAi) embryos. (d) Correlation between centration and pseudocleavage relaxation (left) and centration and myosin transitions (right) in wild-type (blue circles) and PRI-1 (RNAi) embryos (red squares). **First draft complete.**

Figure 2: Maintenance phase biochemistry encodes a stable, attractive steady state with a unique boundary position. (a) CDK-1, (b) ect-2 ts, (c) Charlie’s data.

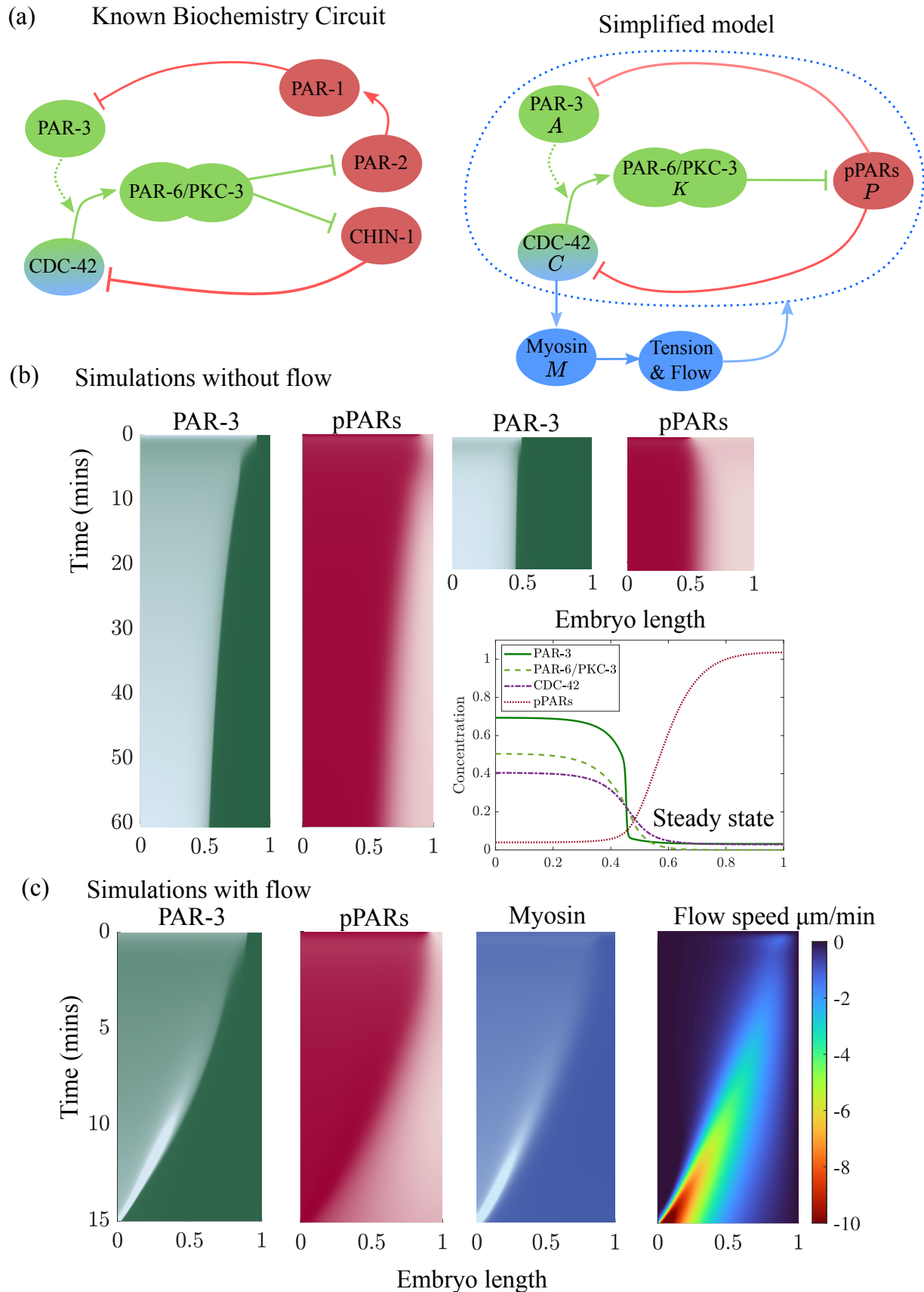
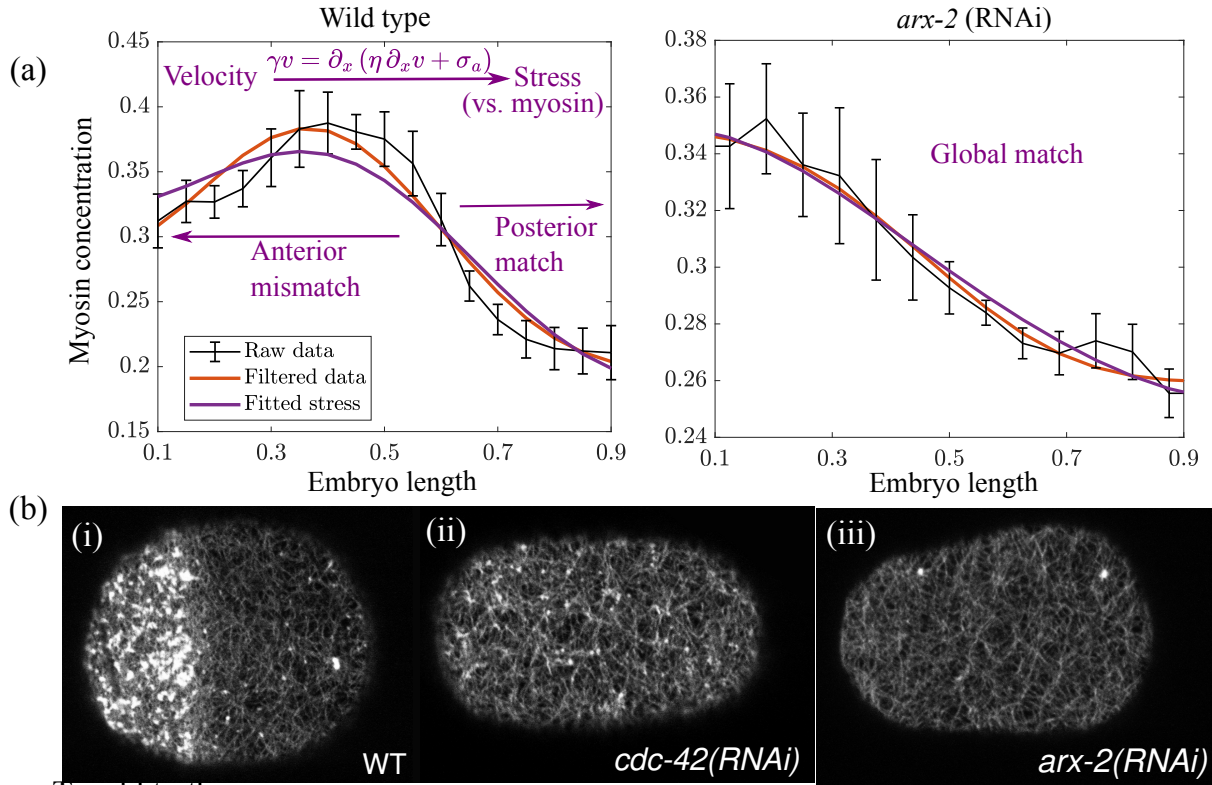


Figure 3: Models based a simple interaction of PAR proteins and myosin can stably maintain a polarity boundary, but cannot explain rescue. (a) Simplified model of PAR protein dynamics, and how it relates to the known system biochemistry (Lang and Munro, 2017). (b) Simulations without flow can maintain a stable boundary but cannot reproduce rescue in a realistic time. These panels show pseudo-kymographs of PAR-3 (green, left) and pPARs (red, right) in rescue (left, the boundary starts at 90% embryo length) and normal maintenance (right, the boundary starts at 50% embryo length) conditions. The bottom plot shows the unique steady state in the model without flow. (c) Simulations with flow lead to a vanishing anterior domain. Shown are pseudo-kymographs of the PAR-3, pPAR, and myosin concentrations over time, as well as the flow speeds. **First draft complete**



To add to this:

Branched actin phenotype with and without nocodazole
Pictures and kymographs

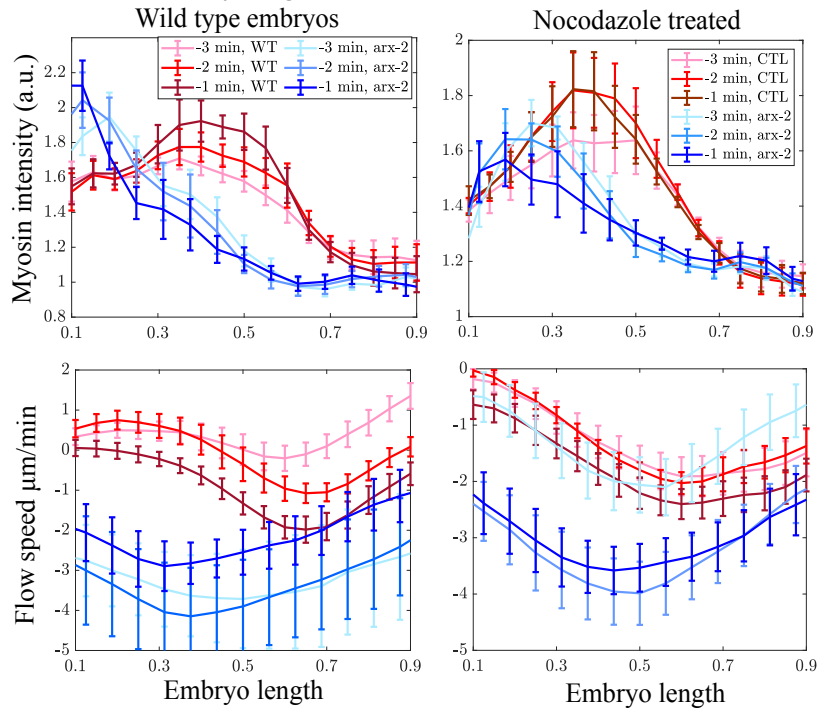


Figure 4: Branched actin acts in the anterior to suppress contractility in wild-type embryos.

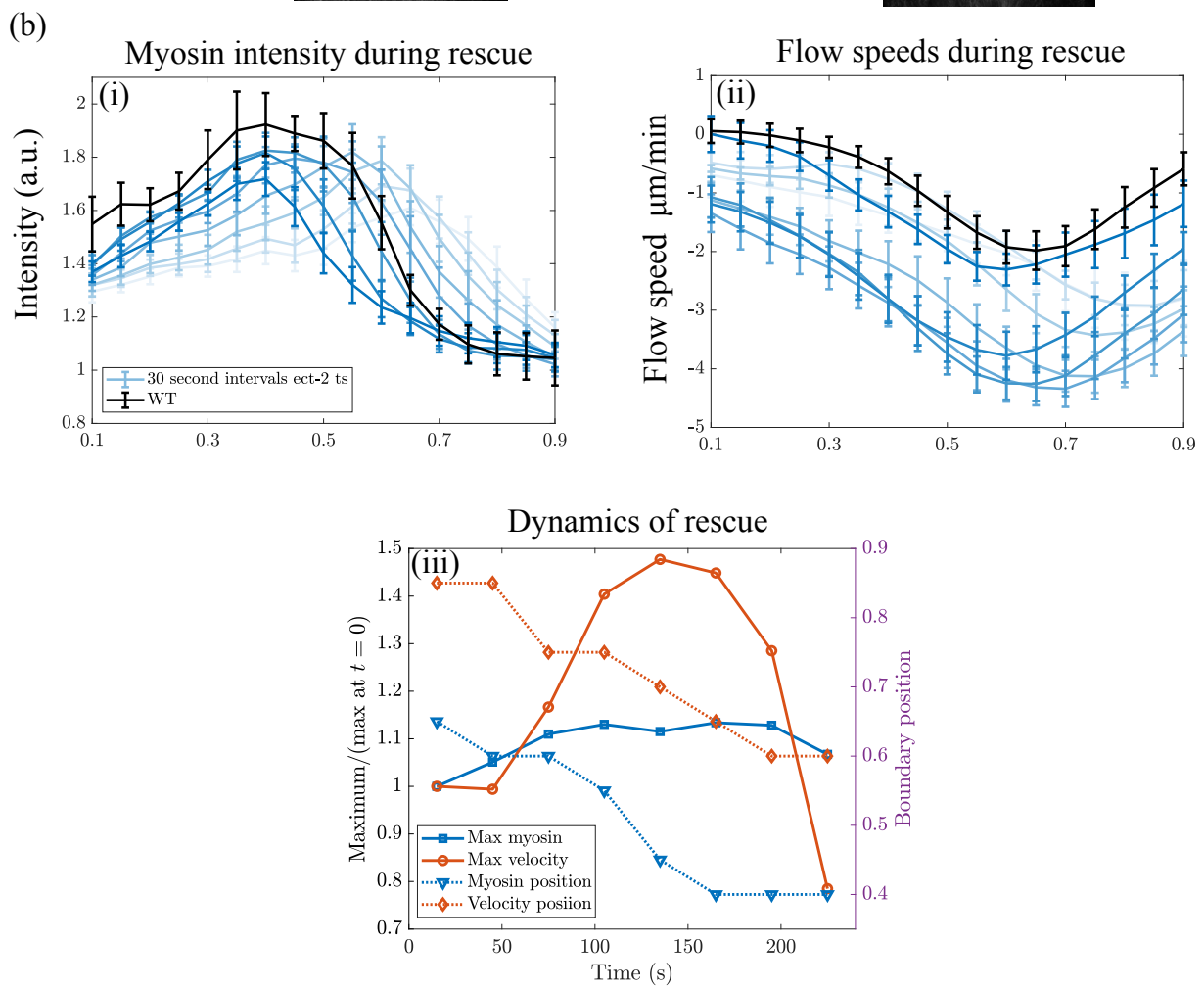
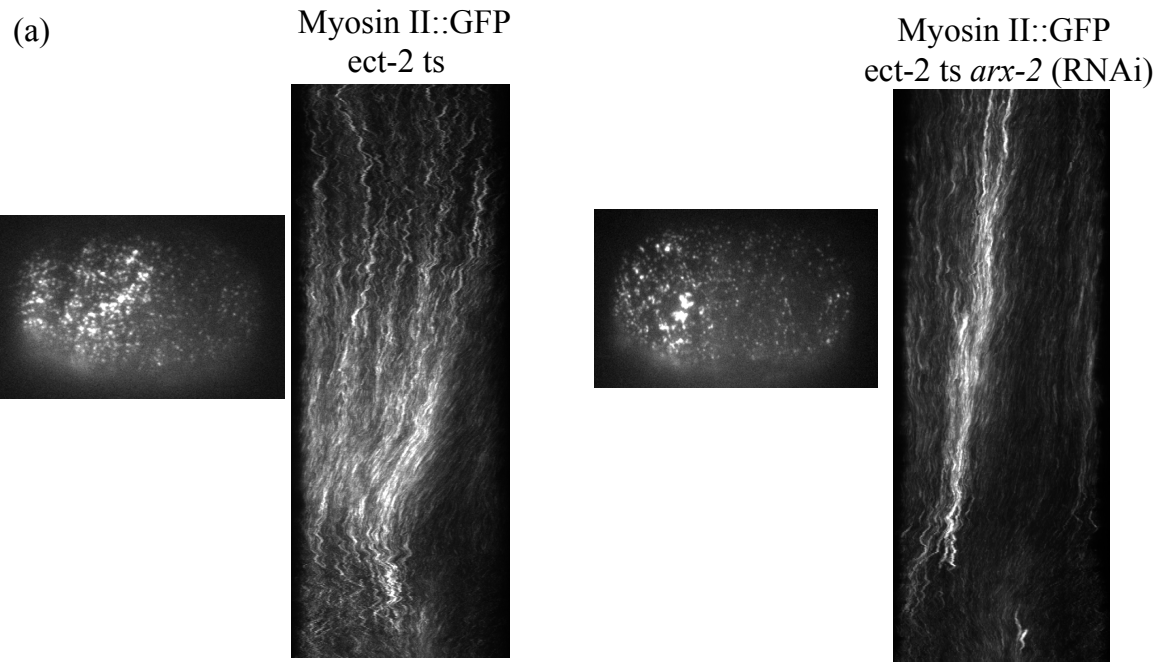
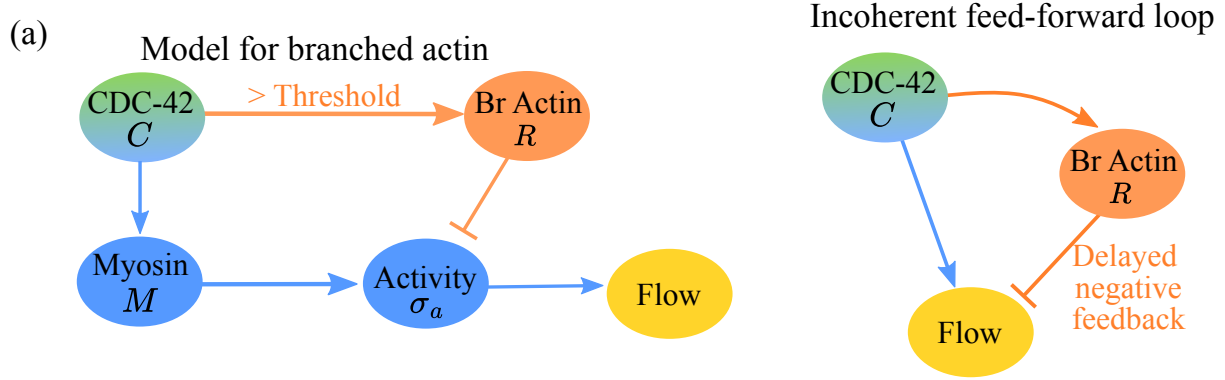


Figure 5: Branched actin acts suddenly to alleviate contractile tension in the anterior during maintenance phase rescue. (a) Still images and kymograph of myosin II (NMY-2::GFP) in ect-2 ts embryos (left) and ect-2 ts embryos with arx-2 (RNAi) (right). (b) Myosin intensity (i) and flow speeds (ii) in ect-2 (ts) embryos (blue lines) compared to wild-type. Data are shown at 30 second intervals using progressively darker lines, and wild-type data in the last minute of maintenance phase are shown in black. (c) Summary of rescue dynamics. Solid lines, governed by the left axis, show the maximum in myosin intensity (blue) and velocity (red), scaled by the value at the onset of maintenance phase ($t = 0$). Dashed lines, governed by the right axis, show the position of the peak in myosin (blue) and velocity (red) over time. **First draft complete.**



(b)

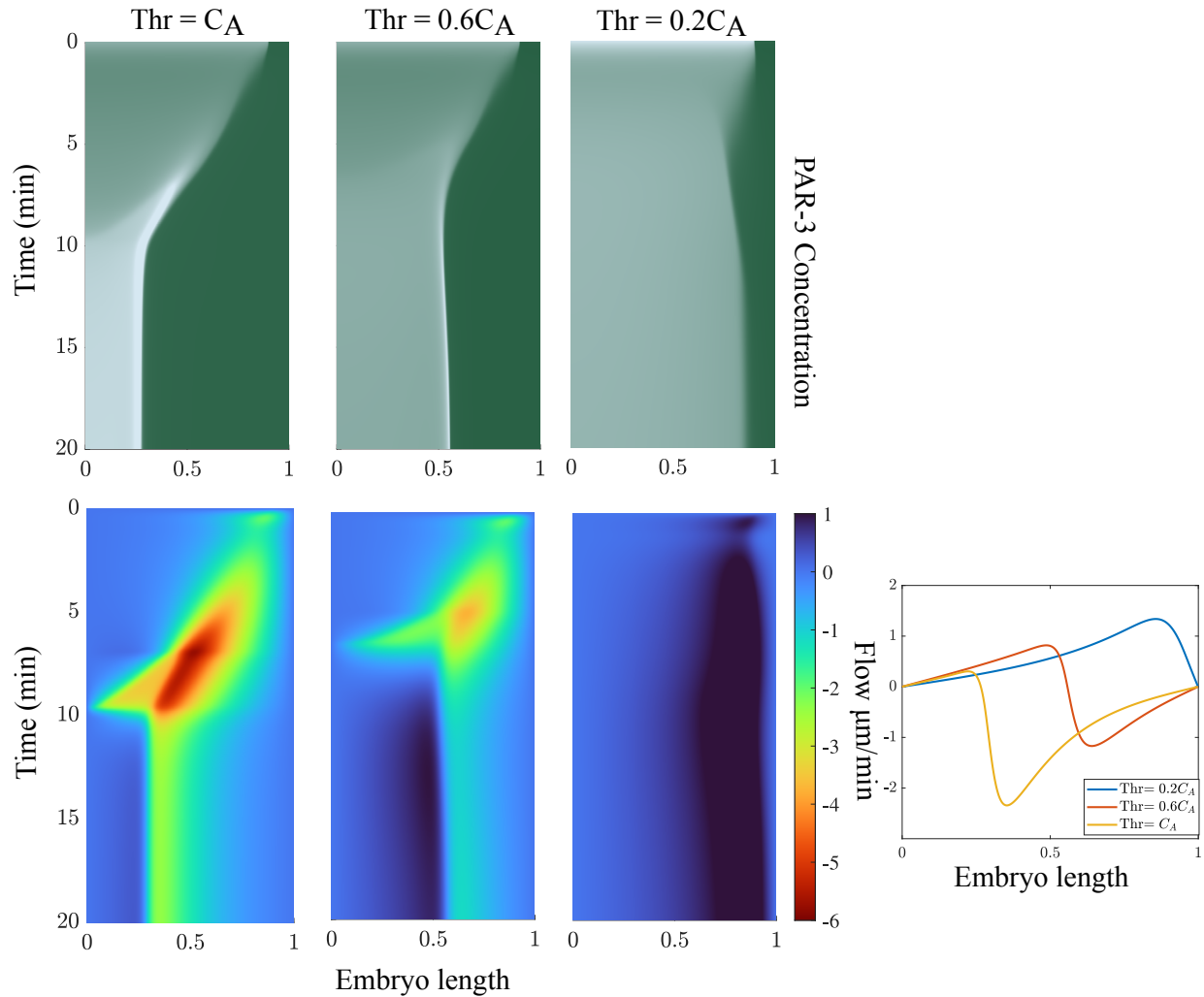


Figure 6: Models that incorporate branched actin successfully reproduce the dynamics of rescue. (a) Extension of the model presented in Fig. 3(a) to account for branched actin. Above a threshold of CDC-42, branched actin is produced and inhibits contractile stress. At its simplest level, these dynamics are an incoherent feed-forward loop (right). (b) Simulations with varying branched actin thresholds show varying degrees of contractility. Shown are kymographs of the PAR-3 domain (top) and flow speeds (bottom) over time. Each column shows a different threshold for branched actin, given in terms of the typical anterior CDC-42 concentration (0.4; see Fig. 3(b)). The steady state flow profiles for each threshold are also shown at bottom right. **First draft complete.**

References

- Donato Aceto, Melissa Beers, and Kenneth J Kemphues. Interaction of par-6 with cdc-42 is required for maintenance but not establishment of par asymmetry in *c. elegans*. *Developmental biology*, 299(2):386–397, 2006.
- Tom Bland, Nisha Hirani, David Briggs, Riccardo Rossetto, KangBo Ng, Neil Q McDonald, David Zwicker, and Nathan W Goehring. Optimized dimerization of the par-2 ring domain drives cooperative and selective membrane recruitment for robust feedback-driven cell polarization. *bioRxiv*, pages 2023–08, 2023.
- Justin S Bois, Frank Jülicher, and Stephan W Grill. Pattern formation in active fluids. *Biophysical Journal*, 100(3):445a, 2011.
- Agathe Chaigne, Clément Campillo, Nir S Gov, Raphaël Voituriez, C Sykes, Marie-Hélène Verlhac, and Marie-Emilie Terret. A narrow window of cortical tension guides asymmetric spindle positioning in the mouse oocyte. *Nature communications*, 6(1):6027, 2015.
- Carrie R Cowan and Anthony A Hyman. Acto-myosin reorganization and par polarity in *c. elegans*. 2007.
- Adrian A Cuenca, Aaron Schetter, Donato Aceto, Kenneth Kemphues, and Geraldine Seydoux. Polarization of the *c. elegans* zygote proceeds via distinct establishment and maintenance phases. 2003.
- Adriana T Dawes and Edwin M Munro. Par-3 oligomerization may provide an actin-independent

- mechanism to maintain distinct par protein domains in the early *caenorhabditis elegans* embryo. *Biophysical journal*, 101(6):1412–1422, 2011.
- Evan B Dewey, Danielle T Taylor, and Christopher A Johnston. Cell fate decision making through oriented cell division. *Journal of developmental biology*, 3(4):129–157, 2015.
- Nathan W Goehring, Philipp Khuc Trong, Justin S Bois, Debanjan Chowdhury, Ernesto M Nicola, Anthony A Hyman, and Stephan W Grill. Polarization of par proteins by advective triggering of a pattern-forming system. *Science*, 334(6059):1137–1141, 2011.
- Bob Goldstein and Ian G Macara. The par proteins: fundamental players in animal cell polarization. *Developmental cell*, 13(5):609–622, 2007.
- Monica Gotta, Mary C Abraham, and Julie Ahringer. Cdc-42 controls early cell polarity and spindle orientation in *c. elegans*. *Current biology*, 11(7):482–488, 2001.
- Peter Gross, K Vijay Kumar, Nathan W Goehring, Justin S Bois, Carsten Hoege, Frank Jülicher, and Stephan W Grill. Guiding self-organized pattern formation in cell polarity establishment. *Nature physics*, 15(3):293–300, 2019.
- Niv Ierushalmi and Kinneret Keren. Cytoskeletal symmetry breaking in animal cells. *Current Opinion in Cell Biology*, 72:91–99, 2021.
- Rukshala Illukkumbura, Nisha Hirani, Joana Borrego-Pinto, Tom Bland, KangBo Ng, Lars Huhatsch, Jessica McQuade, Robert G Endres, and Nathan W Goehring. Design principles for selective polarization of par proteins by cortical flows. *Journal of Cell Biology*, 222(8), 2023.
- Sukriti Kapoor and Sachin Kotak. Centrosome aurora a regulates rhogef ect-2 localisation and ensures a single par-2 polarity axis in *c. elegans* embryos. *Development*, 146(22):dev174565, 2019.
- Amanda J Kay and Craig P Hunter. Cdc-42 regulates par protein localization and function to control cellular and embryonic polarity in *c. elegans*. *Current Biology*, 11(7):474–481, 2001.
- Kraig T Kumfer, Steven J Cook, Jayne M Squirrell, Kevin W Eliceiri, Nina Peel, Kevin F O’Connell, and John G White. Cgef-1 and chin-1 regulate cdc-42 activity during asymmetric division in the *caenorhabditis elegans* embryo. *Molecular biology of the cell*, 21(2):266–277, 2010.

Charles F Lang and Edwin Munro. The par proteins: from molecular circuits to dynamic self-stabilizing cell polarity. *Development*, 144(19):3405–3416, 2017.

Charles F Lang, Alexander Anneken, and Edwin Munro. Oligomerization and feedback on membrane recruitment stabilize par-3 asymmetries in *c. elegans* zygotes. *bioRxiv*, pages 2023–08, 2023.

Rong Li and Bruce Bowerman. Symmetry breaking in biology. *Cold Spring Harbor perspectives in biology*, 2(3):a003475, 2010.

Katrina M Longhini and Michael Glotzer. Aurora a and cortical flows promote polarization and cytokinesis by inducing asymmetric ect-2 accumulation. *Elife*, 11:e83992, 2022.

Jean-Léon Maître, Hervé Turlier, Rukshala Illukkumbura, Björn Eismann, Ritsuya Niwayama, François Nédélec, and Takashi Hiiragi. Asymmetric division of contractile domains couples cell positioning and fate specification. *Nature*, 536(7616):344–348, 2016.

Mirjam Mayer, Martin Depken, Justin S Bois, Frank Jülicher, and Stephan W Grill. Anisotropies in cortical tension reveal the physical basis of polarizing cortical flows. *Nature*, 467(7315):617–621, 2010.

Ani Michaud, Marcin Leda, Zachary T Swider, Songeun Kim, Jiaye He, Jennifer Landino, Jenna R Valley, Jan Huisken, Andrew B Goryachev, George von Dassow, et al. A versatile cortical pattern-forming circuit based on rho, f-actin, ect2, and rga-3/4. *Journal of Cell Biology*, 221(8):e202203017, 2022.

Jonathan B Michaux, François B Robin, William M McFadden, and Edwin M Munro. Excitable rhoa dynamics drive pulsed contractions in the early *c. elegans* embryo. *Journal of Cell Biology*, 217(12):4230–4252, 2018.

Yoichiro Mori, Alexandra Jilkine, and Leah Edelstein-Keshet. Wave-pinning and cell polarity from a bistable reaction-diffusion system. *Biophysical journal*, 94(9):3684–3697, 2008.

Fumio Motegi and Asako Sugimoto. Sequential functioning of the ect-2 rhogef, rho-1 and cdc-42 establishes cell polarity in *caenorhabditis elegans* embryos. *Nature cell biology*, 8(9):978–985, 2006.

Fumio Motegi, Seth Zonies, Yingsong Hao, Adrian A Cuenca, Erik Griffin, and Geraldine Seydoux. Microtubules induce self-organization of polarized par domains in *caenorhabditis elegans* zygotes. *Nature cell biology*, 13(11):1361–1367, 2011.

Edwin Munro and Bruce Bowerman. Cellular symmetry breaking during *caenorhabditis elegans* development. *Cold Spring Harbor perspectives in biology*, 1(4):a003400, 2009.

Edwin Munro, Jeremy Nance, and James R Priess. Cortical flows powered by asymmetrical contraction transport par proteins to establish and maintain anterior-posterior polarity in the early *c. elegans* embryo. *Developmental cell*, 7(3):413–424, 2004.

Camelia G Muresan, Zachary Gao Sun, Vikrant Yadav, A Pasha Tabatabai, Laura Lanier, June Hyung Kim, Taeyoon Kim, and Michael P Murrell. F-actin architecture determines constraints on myosin thick filament motion. *Nature communications*, 13(1):7008, 2022.

Masatoshi Nishikawa, Sundar Ram Naganathan, Frank Jülicher, and Stephan W Grill. Controlling contractile instabilities in the actomyosin cortex. *Elife*, 6:e19595, 2017.

Josana Rodriguez, Florent Peglion, Jack Martin, Lars Hubatsch, Jacob Reich, Nisha Hirani, Alicia G Gubieda, Jon Roffey, Artur Ribeiro Fernandes, Daniel St Johnston, et al. apkc cycles between functionally distinct par protein assemblies to drive cell polarity. *Developmental cell*, 42(4):400–415, 2017.

Anne Sailer, Alexander Anneken, Younan Li, Sam Lee, and Edwin Munro. Dynamic opposition of clustered proteins stabilizes cortical polarity in the *c. elegans* zygote. *Developmental cell*, 35(1):131–142, 2015.

Stephanie Schonegg and Anthony A Hyman. Cdc-42 and rho-1 coordinate acto-myosin contractility and par protein localization during polarity establishment in *c. elegans* embryos. 2006.

Yu Chung Tse, Michael Werner, Katrina M Longhini, Jean-Claude Labbe, Bob Goldstein, and Michael Glotzer. Rhoa activation during polarization and cytokinesis of the early *caenorhabditis elegans* embryo is differentially dependent on nop-1 and cyk-4. *Molecular biology of the cell*, 23(20):4020–4031, 2012.

Qing Yang, Xiao-Feng Zhang, Thomas D Pollard, and Paul Forscher. Arp2/3 complex-dependent actin networks constrain myosin ii function in driving retrograde actin flow. *Journal of Cell Biology*, 197(7):939–956, 2012.

Seth Zonies, Fumio Motegi, Yingsong Hao, and Geraldine Seydoux. Symmetry breaking and polarization of the *c. elegans* zygote by the polarity protein par-2. *Development*, 137(10):1669–1677, 2010.